The Astrophysical Journal, 975:155 (7pp), 2024 November 10 https://doi.org/10.3847/1538-4357/ad8232

Joint Observation of a Series of Magnetic Holes by Tianwen-1 and MAVEN on Mars

T. Y. Zhou[1,2], H. S. Fu[1,2], Z. Z. Guo[1,2], J. B. Cao[1,2], Y. M. Wang[3,4], W. D. Fu[1,2], Z. Wang[1,2], and M. Ge[1,2]
[1] School of Space and Environment, Beihang University, Beijing, People's Republic of China; huishanf@gmail.com
[2] Key Laboratory of Space Environment Monitoring and Information Processing, Ministry of Industry and Information Technology, Beijing, People's Republic of China
[3] Deep Space Exploration Laboratory/School of Earth and Space Sciences, University of Science and Technology of China, Hefei, People's Republic of China
[4] CAS Center for Excellence in Comparative Planetology/CAS Key Laboratory of Geospace Environment/Mengcheng National Geophysical Observatory, University of Science and Technology of China, Hefei, People's Republic of China
Received 2024 September 3; revised 2024 September 25; accepted 2024 September 30; published 2024 October 31

Abstract

Magnetic holes (MHs) are transient magnetic structures responsible for energy conversion in space plasma. Using single-spacecraft measurements from Mars Atmosphere and Volatile EvolutioN (MAVEN), the existence of MHs on Mars has been confirmed. However, due to the limitations of single-spacecraft observations, significant uncertainty also arises on the identification of the spatial scale and 3D geometry of MHs. In this study, we report a series of MHs successively detected by Tianwen-1 near the high-latitude magnetopause and by the MAVEN spacecraft near the subsolar magnetopause. The large separation between Tianwen-1 and MAVEN ($\sim 4\,R_M$) suggests these MHs are macroscale structures extending along the axial direction. Additionally, we observe whistler waves generated by electron perpendicular anisotropy in one of the macroscale MHs. This study is the first joint observation of Martian MHs, shedding light on the research of transient magnetic structures on Mars.

Unified Astronomy Thesaurus concepts: Mars (1007); Solar wind (1534); Space plasmas (1544)

1. Introduction

Magnetic holes (MHs), also referred to as magnetic decreases, are transient magnetic structures (H. S. Fu et al. 2013a, 2017, 2019, 2020a) characterized by depressions in magnetic field strength accompanied by increases in plasma density (H. S. Fu et al. 2011a; S. T. Yao et al. 2019; K. Liu et al. 2020; Y. Yu et al. 2022a, 2022b). MHs are quasi-symmetric, pressure-balanced structures that play a significant role in energy conversion (Y. Xu et al. 2018; Z. Wang et al. 2019, 2020; Y. Yu et al. 2022a; Z. Wang et al. 2024) and particle transport. The formation mechanisms of MHs involve various physical processes, including mirror-mode instabilities (B. T. Tsurutani et al. 1982; T. L. Zhang et al. 2008; T. Xiao et al. 2010, 2014), sheetlike equilibrium structures, solitary waves (L. F. Burlaga & J. F. Lemaire 1978), and interchange instabilities (Y. Yu et al. 2022b). MHs have various spatial scales from large MHD scales to kinetic scales (B. T. Tsurutani et al. 2011; L. Yu et al. 2021, 2022).

As one kind of transient magnetic structure (S. Y. Huang et al. 2012, 2015; K. Jiang et al. 2020, 2024), MHs widely exist in the space plasma, including the magnetosheaths (B. T. Tsurutani et al. 1982; S. P. Joy et al. 2006; S. Y. Huang et al. 2017a), the magnetospheres of planets (M. A. Balikhin et al. 2012; Z. Zhima et al. 2015; H. S. Fu et al. 2020b), the terrestrial magnetotail (S. Y. Huang et al. 2019), the terrestrial foreshock region (S. Y. Huang et al. 2022), the magnetosphere of comets (C. T. Russell et al. 1987; E. A. Lucek et al. 1999; J. Soucek et al. 2008; Y. Y. Liu et al. 2019), and the solar wind (J. M. Turner et al. 1977; T. L. Zhang et al. 2008). MHs have been detected on all terrestrial planets. The MHs are usually observed together with the electron vortex (S. Y. Huang et al. 2017b; L. Yu et al. 2024) and play an important role in energy dissipation (Z. Wang et al. 2023). On Mars, they are found throughout the Martian magnetosphere, including in the bow shock (H. Madanian et al. 2020; G. Q. Wang et al. 2021), magnetosheath (S. Y. Huang et al. 2021; M. Wu et al. 2021; Y. Chen et al. 2022), and magnetotail. These Martian MHs play a crucial role in particle transport, energy excitation, and energy dissipation.

Mars has only an induced magnetic field, rendering its magnetic environment unstable (A. F. Nagy et al. 2004; R. Ramstad et al. 2020; Z. Z. Guo et al. 2021, 2022). Previous research on MHs on Mars has primarily relied on single-spacecraft observations. A single spacecraft can conduct statistical studies or event analyses of MHs on Mars, but this approach has inherent limitations. Due to the 3D structure of MHs, the signals detected by a single spacecraft are highly dependent on the satellite's position and trajectory as it passes through the MH. This can lead to significant discrepancies between the estimated size and properties of the MH based on the spacecraft's data and the actual conditions in space. For example, a satellite might pass through a large MH, but due to its specific trajectory, the data could misleadingly suggest a smaller MH, leading to an incorrect interpretation that could affect the research outcomes. Tianwen-1 and Mars Atmosphere and Volatile EvolutioN (MAVEN) have different orbits and operational altitudes. When utilizing the combined observations from MAVEN and Tianwen-1, by comparing signals from both spacecraft, we can consider more information than would be possible with a single spacecraft, resulting in more reliable and accurate estimation of MHs' sizes and traversal paths. This approach enhances our ability to identify and understand large-scale MHs in the Martian space environment.

In this study, we observe a series of MHs in the solar wind in the upper reaches of the atmosphere of Mars using simultaneous measurements from Tianwen-1 and MAVEN.

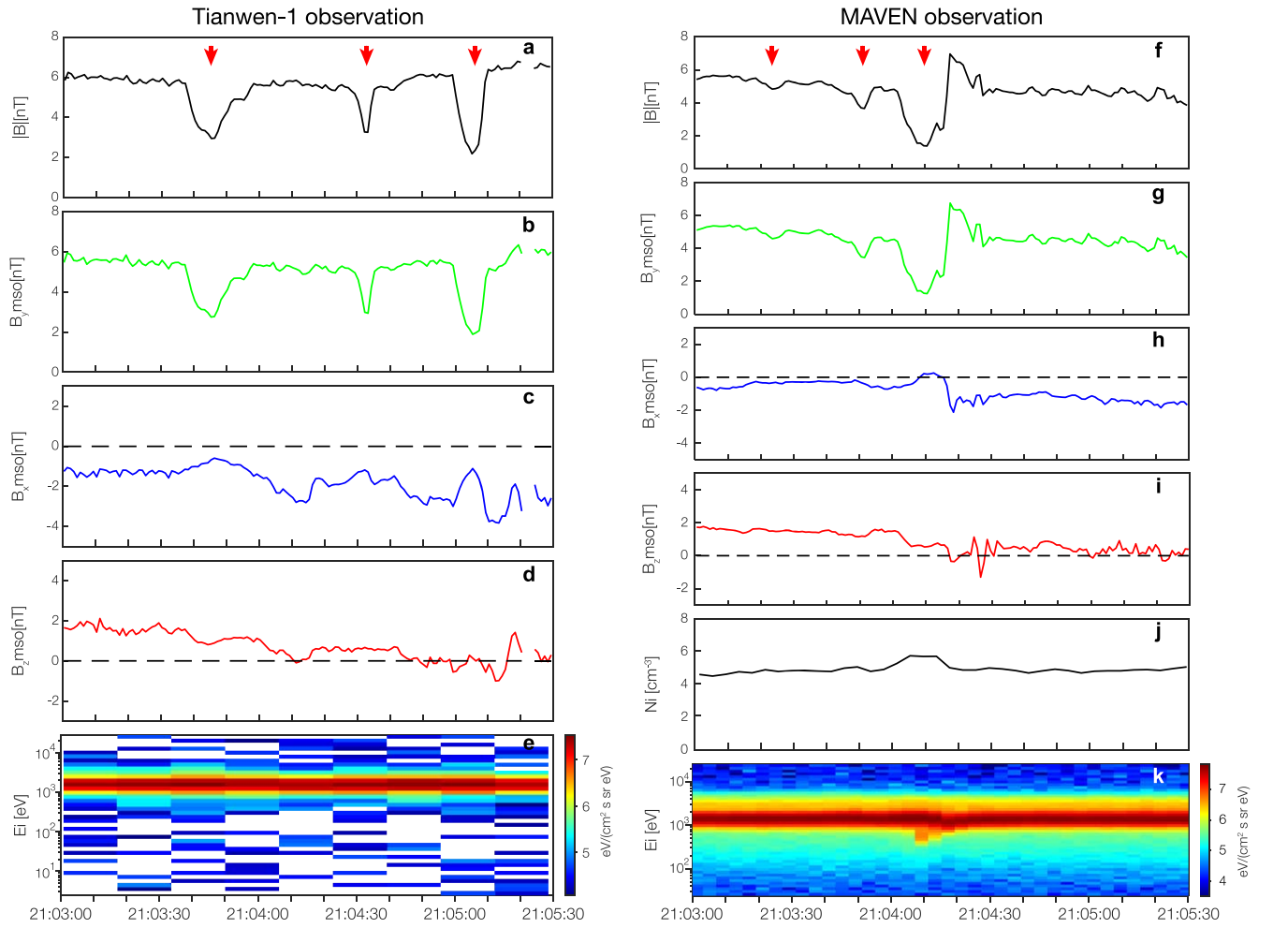

Figure 1. Overview of measurements from the two satellites, Tianwen-1 and Mars Atmosphere and Volatile Evolution (MAVEN), on 2021 December 16. (a) The total magnetic field measured by Tianwen-1; (b) the B_y component measured by Tianwen-1; (c) the B_x component measured by Tianwen-1; (d) the B_z component measured by Tianwen-1; (e) the ion spectrum measured by Tianwen-1; (f) the total magnetic field measured by MAVEN; (g) the B_y component measured by MAVEN; (h) the B_x component measured by MAVEN; (i) the B_z component measured by MAVEN; (j) the ion density measured by MAVEN; (k) the ion spectrum measured by MAVEN. MSO represents the Mars Solar Orbital joints. The $X_{\rm MSO}$ is directed from the center of the planet toward the center of the Sun, $Y_{\rm MSO}$ points opposite to the direction of Mars's orbital velocity component perpendicular to $X_{\rm MSO}$, and $Z_{\rm MSO}$ completes the right-handed system.

2. Data and Observations

In this study, we utilized data from the Tianwen-1 (W. X. Wan et al. 2020) and MAVEN (B. M. Jakosky et al. 2015) missions. The Tianwen-1 orbiter's Mars Orbiter Magnetometer (Y. Y. Liu et al. 2020; Y. Wang et al. 2023; Z. Zou et al. 2023; G. Q. Wang et al. 2024) measures the magnetic field of Mars, operating at a sampling frequency of 32 Hz near periareon (approximately 265 km from the surface) and apoareon (approximately 11,945.6 km from the surface) and at 1 Hz elsewhere. The Mars Ion and Neutral Particle Analyzer, which detects ions and neutral particles around Mars, has a time resolution of ion detection up to 4 s. For this study, hydrogen ion (H^+) data from the MOD-01 package were utilized (L. Kong et al. 2020). Diverse data from MAVEN were also utilized, including magnetic field measurements from the magnetometer with a sampling frequency of 1/32 Hz (J. E. P. Connerney et al. 2015), ion data from the Solar Wind Ion Analyzer with a time resolution of 4 s (J. S. Halekas et al. 2015), and electron data from the Solar Wind Electron Analyzer with a time resolution of 2 s (D. Mitchell et al. 2016). All data in this study are expressed in Mars Solar Orbit (MSO) coordinates: X-points from Mars toward the Sun, Y-points opposite Mars's orbital velocity (perpendicular to X), and Z-points orthogonal to both X and Y.

The event of interest occurred on 2021 December 16, between 21:03:00 and 21:05:30 UT. During this period, Tianwen-1 was positioned at $[-0.35, -1.70, -3.28]\,R_{\rm M}$ in MSO coordinates, while MAVEN was located at $[1.64, -0.28, -0.34]\,R_{\rm M}$, near the subsolar magnetopause. Figure 1 presents the measurements from Tianwen-1 (left) and MAVEN (right) over the same time frame. The left panels, from top to bottom, show the total magnetic field measured by Tianwen-1, followed by the y-, x-, and z-direction components of the magnetic field, and the ion spectrum. The right panels, from top to bottom, display the total magnetic field measured by MAVEN, the y-, x-, and z-direction components of the magnetic field, the ion density, and the ion spectrum. In Figure 1, the magnetic field data we used have a frequency of 1 Hz (both Tianwen-1 and MAVEN).

We observed three instances of total magnetic field reductions in the Tianwen-1 data, which we interpret as three consecutive MHs. The decreases in the magnetic field primarily occurred in the y-component (about 3–4 nT), indicating that

the principal orientation of these MHs is along the *y*-axis. These reductions are marked with red arrows in Figure 1(a). Correspondingly, there are also slight reductions in the *x*-component of the magnetic field (about 1–2 nT), while the *z*-component shows no significant changes, suggesting that these MHs are tilted along the *x*-axis. As shown by the ion spectrum in Figure 1(e), the Tianwen-1 spacecraft remained within the solar wind throughout the entire period. Notably, during this period, three instances of magnetic field weakening are also observed in the total magnetic field data from MAVEN (Figure 1(f)), which are marked with red arrows. As shown by the ion spectrum in Figure 1(k), MAVEN was also within the solar wind during this period, consistent with Tianwen-1. However, in this event, the time resolution of the ion data provided by Tianwen-1 is 16 s, which is too low. We did not compute the ion moment. Additionally, the provided ion data do not include the transformation matrix between the instrument coordinate system and the MSO coordinate system, so we did not compute the ion velocity. The first two magnetic field dips observed by MAVEN were small, around 1 nT, while the third was relatively large, about 4 nT. At the corresponding times, the particle density also increased, indicating that these are three consecutive MHs. Similarly, these dips primarily occurred in the *y*-direction, consistent with the characteristics observed in the Tianwen-1 measurements. Within such a short period, it would be highly coincidental for both spacecraft, even with their different orbits, to observe three consecutive MHs in the solar wind with the same primary orientation in the *y*-direction. Therefore, we believe these are the same three consecutive MHs, all aligned along the *y*-axis. We will describe in detail below how these two orbiters passed through this continuous series of MHs through a comparative analysis of the measurement signals from two satellites. According to our calculations, the DepthMH (an index for determining a magnetic hole, $\mathrm{DepthMH} = 1 - B_{\mathrm{min}}/B_{\mathrm{background}}$) of the three MHs detected by Tianwen-1 are 51.9%, 46.8%, and 64.3%, respectively, while the results from MAVEN are 14.7%, 22.7%, and 71.4%; all more than 10% (S. Y. Huang et al. 2021). The $\Delta\varphi$ (the angle between the magnetic field directions at the MHs' two edges) of the three MHs detected by Tianwen-1 are 6°.7, 0°.3, and 10°.0, respectively, while 1°.2, 4°.5, and 20°.0, respectively, are detected by MAVEN. When $\Delta\varphi < 30°$, we can confirm that the structure is a linear MH rather than a current sheet (M. Wu et al. 2021). These characteristics are consistent with the criteria used in other studies to identify MHs. Therefore our judgment is reasonable.

Figures 2(a)–(c) illustrate the positions of the two satellites in MSO coordinates. Figure 2(d) shows the three components of the solar wind velocity as measured by MAVEN. Figure 2(e) presents the total magnetic field data from MAVEN, while Figure 2(f) shows the total magnetic field data from Tianwen-1. In Figures 2(e) and (f), the three shaded areas represent the time periods when the satellites passed through the MHs. Between Figures 2(e) and (f), we use three colored arrows to indicate the time differences between the two satellites passing through each MH. The values represent the estimated time differences between the points of the weakest magnetic field. Figures 2(g)–(i) present schematics to explain why there is a delay in the signal from the Tianwen-1 detecting each MH. Since the actual conditions of the MHs in space are unknown, including their exact size and shape, the diagrams we provide are schematic representations. They illustrate the process and positions of the satellites passing through the MHs, intended to explain the delay in Tianwen-1's detection of the MHs. Compared to Tianwen-1, the MAVEN satellite is positioned closer to the Sun, with a difference of approximately 2 R_{M} in the *x*-direction. Since the primary direction of the solar wind flow velocity is in the -*x*-direction, the MHs moving with the solar wind will encounter MAVEN first. The distance between Tianwen-1 and MAVEN is approximately 1.4 R_{M} in the *y*-direction and 3 R_{M} in the *z*-direction, resulting in a straight-line distance of about 3.9 R_{M} between the two satellites. We believe that both satellites passed through the same MHs, suggesting that the sizes of these MHs are at least 3.9 R_{M}. The local proton gyroradius (γ_ρ) can be estimated as $\gamma_\rho = \frac{144 * \sqrt{T_i}}{B}$, where T_i represents the proton temperature, measured in eV, and B represents the magnetic field strength, measured in nT. The local proton gyroradius is approximately 215 km, indicating that the sizes of these MHs are at least 62 γ_ρ. Previous studies on the sizes of MHs on Mars have shown that they can reach up to 300 γ_ρ, with the vast majority being smaller than 50 γ_ρ (H. Madanian et al. 2020). However, a significant proportion of MHs still fall within the range of 50–100 γ_ρ. This suggests that the sizes of the MHs estimated from the observations of the two satellites are reasonable. The solar wind velocity measured by the MAVEN satellite in Figure 2(d) remains stable throughout the entire period. The main component of the solar wind velocity is along the *x*-axis, at approximately $-500\,\mathrm{km\,s^{-1}}$, with a speed of about $100\,\mathrm{km\,s^{-1}}$ in the *y*-direction and nearly zero in the *z*-direction. MHs propagate with the solar wind toward Mars, primarily in the -*x*-direction. However, we observed that the time intervals between the two satellites passing through the MHs vary with each instance, gradually increasing over time. These intervals are larger than what would be expected based on the distance between the satellites. Additionally, the magnitude of magnetic field weakening differs with each passage of the same MH. To illustrate this phenomenon, we have created three schematic diagrams.

First, the scenario of the two satellites passing through the first MH corresponds to the schematic in Figure 2(g). MAVEN passed through the first MH from approximately 21:03:19 to 21:03:28 UT, as indicated by the blue shaded area in Figure 2(e). Similarly, Tianwen-1 crossed the first MH from around 21:03:38 to 21:03:59 UT, as shown by the blue shaded region in Figure 2(f), with an interval of about 22 s between these two passages. MAVEN observed a relatively small dip in the magnetic field, which we attribute to the satellite passing through the neck of the MH, whereas Tianwen-1 observed a larger dip, suggesting it passed through the belly of the MH. This difference in crossing locations resulted in different magnetic field strengths being observed. This situation highlights the advantage of joint observations. If only one satellite's data were considered, the MH size derived from MAVEN's data might be as small as 1 R_{M}, while the size from Tianwen-1 could be around 2 R_{M}. Both estimates are significantly smaller than the minimum size of 3.9 R_{M} that we obtained from the joint observations.

Considering only the solar wind velocity in the *x*-direction, the MH would have moved approximately 3 R_{M} toward Mars with the solar wind during these 22 s, while the two satellites were separated by about 2 R_{M} in the *x*-direction. Therefore, the MH should have been detected earlier by Tianwen-1. Figure 2(g) explains why the MH signal was detected later by Tianwen-1.

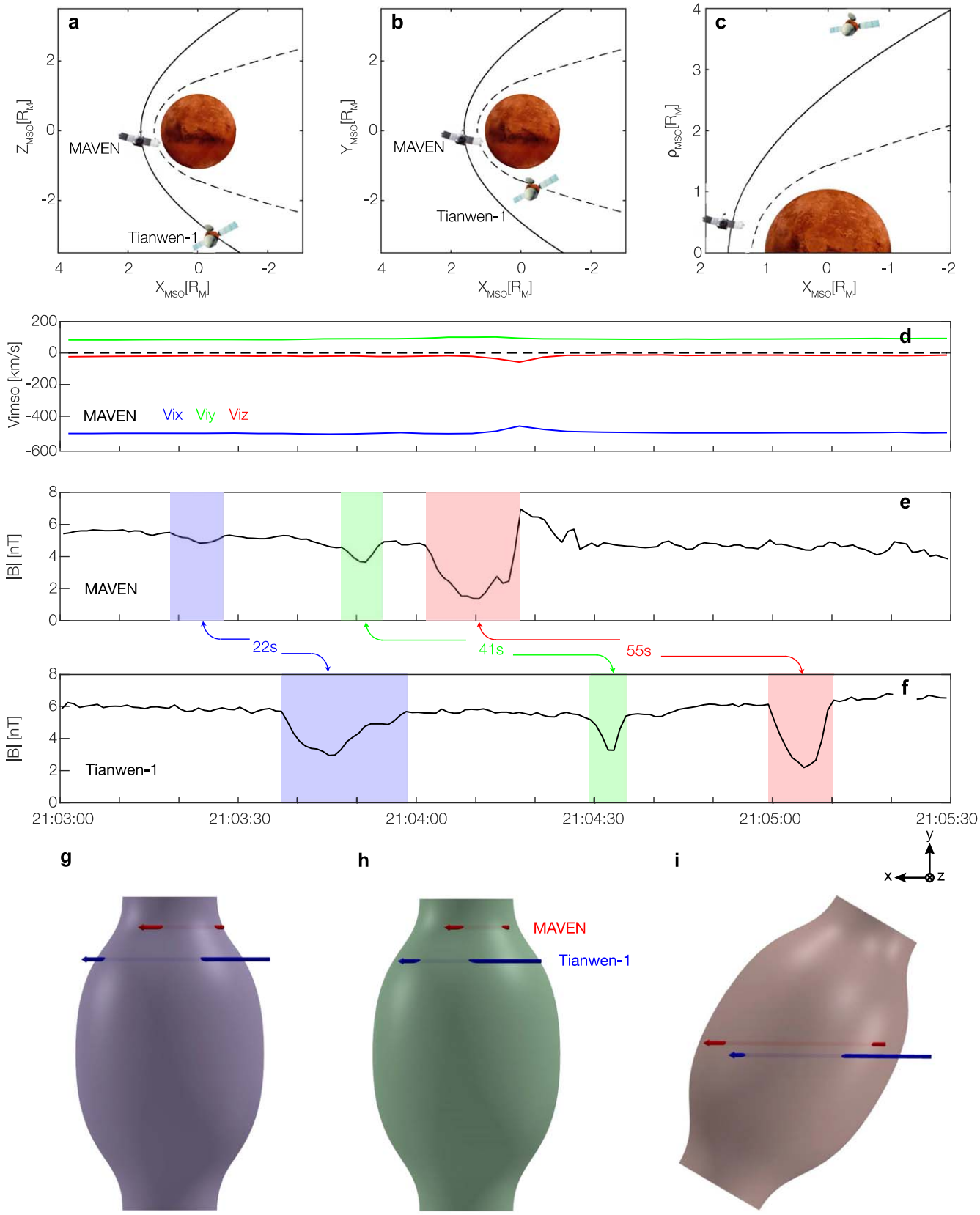

Figure 2. The positions of the two satellites, comparison of the MH signals, and schematic illustrations of the satellites crossing MHs. (a) The locations of MAVEN and Tianwen-1 in the X_{MSO}–Z_{MSO} plane; (b) the locations of MAVEN and Tianwen-1 in the X_{MSO}–Y_{MSO} plane; (c) the locations of MAVEN and Tianwen-1 in the X_{MSO}–ρ_{MSO} plane, $\rho = (Y^2 + Z^2)^{1/2}$; (d) the V_x, V_y, and V_z components of the proton velocity; (e) the total magnetic field measured by MAVEN; (f) the total magnetic field measured by Tianwen-1; (g), (h), (i) schematic illustrations of the satellites crossing MHs, where the red arrows represent the trajectory of MAVEN and the blue arrows represent the trajectory of Tianwen-1.

We believe that the main direction of the MH is along the *y*-axis and that the MH is a 3D structure. The differences in the *y*- and *z*-directions between MAVEN and Tianwen-1 resulted in varying spatial positions as they passed through the MH, causing a delay in the signal detection. In Figure 2(g), the red and blue arrows represent the trajectories of MAVEN and Tianwen-1, with the starting points of the arrows marking the initial positions of each satellite. Since the satellites' velocities are small compared to the solar wind flow speed, we treat the satellites as stationary and consider the MHs as moving toward the satellites with the solar wind. Here, "trajectories" refers to the paths of the satellites relative to the MHs. MAVEN passed through the neck of the MH and observed it first. Tianwen-1, positioned on the -*y* and -*z* sides relative to MAVEN, passed through the off-center belly of the MH, resulting in a certain distance in the *x*-direction. The initial separation between the satellites in the *x*-direction, combined with the different positions of the MH during their crossings, caused a delay in Tianwen-1's observation of the MH's signal.

The scenario of the satellites passing through the second MH is somewhat analogous to the first MH. In Figure 2(e), the green shaded area represents the time period from 21:03:48 to 21:03:54 UT, during which MAVEN passed through the second MH. In Figure 2(f), the green shaded area represents the time period from 21:04:29 to 21:04:35 UT, during which Tianwen-1 passed through the same MH. In this case, MAVEN passed through the neck of the MH, while Tianwen-1 passed through the belly of the MH. The time interval between the two passages was approximately 41 s. During this interval, the MH moved about 6 R_M in the *x*-direction with the solar wind. Figure 2(h) illustrates this situation. As Tianwen-1 passed through the second MH, it was in a more off-center position relative to MAVEN, resulting in a greater distance for detecting the MH signal. Consequently, the MH needed to move farther to align with Tianwen-1's position, leading to the observed 41 s delay before Tianwen-1 detected the MH.

The situation with the third MH differs from the previous ones. In Figure 2(e), the red shaded area represents the time period from 21:04:02 to 21:04:18 UT, during which MAVEN passed through the third MH. In Figure 2(f), the red shaded area corresponds to the time period from 21:05:00 to 21:05:10 UT, when Tianwen-1 passed through the same MH. During these passages, both satellites detected a significant weakening of the magnetic field of approximately 4 nT. This observation suggests that both satellites passed through the belly of the third MH. The time interval between their crossings was 55 s. After the MH encountered MAVEN, it needed to travel an additional 8 R_M before reaching Tianwen-1. Figures 1(c) and (h) show a decrease in magnetic field strength along the *x*-direction during the third MH, though this decrease is less pronounced compared to the *y*-direction. Therefore, we infer that the primary direction of the third MH is along the *y*-direction, with some components extending in the *x*-direction, as depicted in the schematic in Figure 2(i). The inclination of the MH in the *x*-direction required it to move farther to align with Tianwen-1. Three factors contributed to the delay in Tianwen-1 detecting the MH signal: the tilt of the MH, the initial difference in the *x*-direction positions of the satellites, and the off-center crossing due to differences in the *y*- and *z*-directions. Tianwen-1 was positioned more eccentrically and closer to the edge of the MH compared to MAVEN. The combined effect of these factors resulted in a 55 s delay for Tianwen-1 to detect the MH.

3. Discussion

In Figure 1, we observe several fluctuations in the magnetic field. When MAVEN passed through the third MH, there was an enhancement in the ion flux. Figure 3(a) shows MAVEN's measurements of the total magnetic field, while Figure 3(b) displays the power spectral density of the total magnetic field. The black curve represents low-hybrid frequency f_{lh}, and the pink curve represents 0.1 times the electron cyclotron frequency f_{ce}. Both f_{lh} and f_{ce} are derived from the 32 Hz magnetic field data. Between approximately 21:04:08 and 21:04:13 UT, inside the third MH, there was a significant increase in power spectral densities above the 0.1 electron cyclotron frequency, marked by a black dashed line. To determine the wave mode, we processed the magnetic field data using the singular value decomposition (SVD) method, obtaining the wave normal angle (WNA), planarity, and ellipticity (O. Santolík et al. 2003). The WNAs are notably small, almost all below 20° (Figure 3(c)), indicating that these waves propagate quasi-parallel. The planarity values are close to 1 (Figure 3(d)), confirming that the WNAs and ellipticity features derived from SVD are reliable. The ellipticity values are around 1 (Figure 3(e)), suggesting right-hand circular polarization. All these characteristics, including the propagation angle and polarization, are consistent with the properties of whistler waves (S. Y. Huang et al. 2018). Whistler waves propagate along the direction of the magnetic field lines. The wave characteristics observed in space may be influenced by Doppler shift effects (D. A. Brain et al. 2002). Since the main direction of the magnetic field is along the *y*-axis and the solar wind velocity is primarily in the -*x*-direction, the wave propagation direction and ion velocity direction may be nearly perpendicular, indicating that the solar wind has little effect on the wave frequency.

Between approximately 21:04:18 and 21:04:22 UT, after the third MH, the phase-space density (PSD) of the total magnetic field also shows a significant increase in the frequency range between the f_{lh} and $0.1^{*}f_{ce}$. During this period, the WNAs are about 45°, and the ellipticity values are close to 1, suggesting right-hand circular polarization. We identify these waves as Alfvén whistler waves.

Considering that whistler waves may be caused by perpendicular anisotropy (X. Zhang et al. 2019), we examined the electron properties of the event. In Figure 3(f), red and blue rectangles represent the time periods when whistler waves and the background solar wind periods appeared, respectively, above the electron spectrum. The red rectangle indicates the period from 21:04:08 to 21:04:13 UT, while the blue rectangle represents the period from 21:04:30 to 21:05:10 UT. We observe increases in electron energy (H. S. Fu et al. 2011b, 2012, 2013b) both within the MH and in the region where Alfvén whistler waves were detected outside the MH. The PSD of electrons within the MH is shown in Figure 3(g), and in the solar wind in Figure 3(h). The blue lines represent the PSD in the parallel direction, while the red lines represent the PSD in the perpendicular direction. The perpendicular direction is defined by pitch angles between 67°.5 and 112°.5, while the parallel direction covers pitch angles from 0° to 67°.5 and 112°.5 to 180°. In Figure 3(g), it is evident that the PSD of electrons in the perpendicular direction is higher than in the parallel direction, particularly between 30 and 100 eV, indicating perpendicular anisotropy during the occurrence of whistler waves. In Figure 3(h), below 50 eV, the PSD of

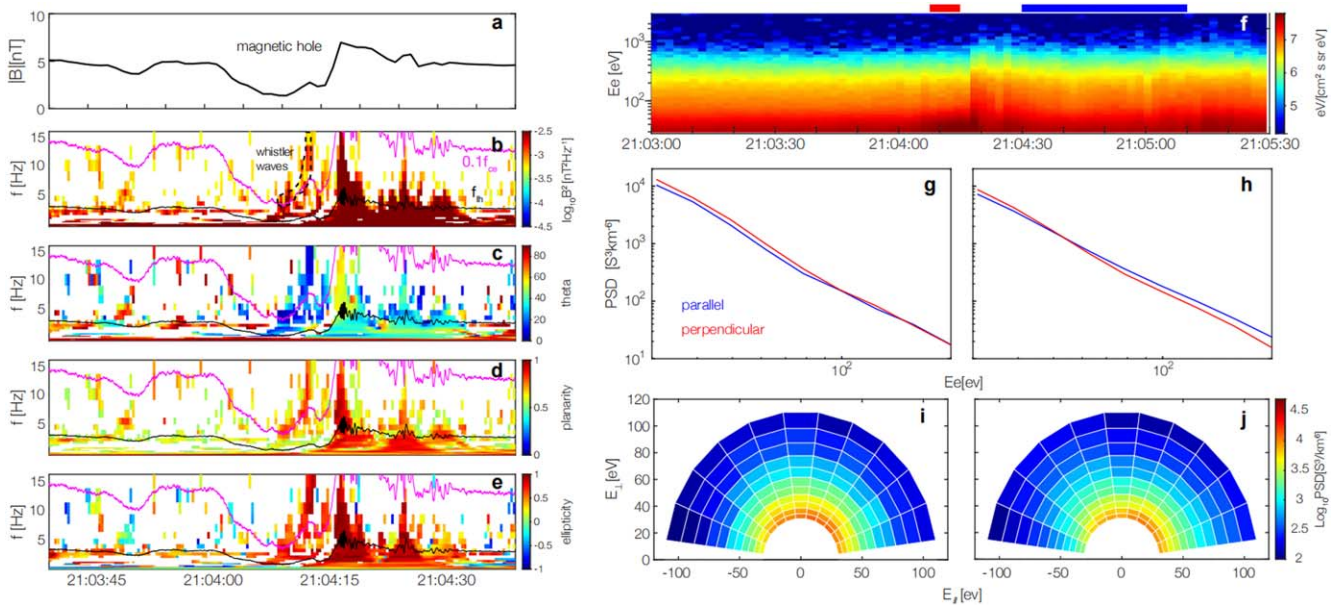

Figure 3. Polarization analyses of the magnetic field fluctuation and electronic distribution, measured by MAVEN. (a) $|B|$. (b) Spectrogram of $|B|$, where the black curve denotes low frequency and the pink curve denotes 0.1 times electron cyclotron frequency. (c) Wave normal angle (WNA). (d) Planarity of waves. (e) Ellipticity of waves. The WNA varies from 0° to 90°. 90° denotes that the waves propagate perpendicular to the ambient magnetic field, and 0° denotes that the waves propagate parallel or antiparallel to the ambient magnetic field. The value of planarity varies between 0 and 1, with values close to 1 indicating that the other polarization parameters calculated by the SVD method are reliable. The value of ellipticity varies between −1 and 1, with 1 denoting right-hand polarization, −1 denoting left-hand polarization, and 0 denoting linear polarization. (f) The electronic spectra. (g) The parallel PSD and the perpendicular PSD as a function of electron energy inside the MH region. (h) The parallel PSD and the perpendicular PSD as a function of electron energy in the background solar wind. (i) Electronic distribution inside the MH region. (j) Electron distribution inside the solar wind region.

electrons in the perpendicular direction exceeds that in the parallel direction, while the opposite is true above 50 eV. Figure 3(i) illustrates the electron distribution during the whistler wave occurrence (red box) within the MH, while Figure 3(j) shows the electron distribution of the background solar wind (blue box). The perpendicular anisotropy is more pronounced in the MH, where the whistler waves are present. We conclude that the whistler waves are likely excited by this perpendicular anisotropy.

4. Summary

This paper reports on a series of MHs observed in the upstream solar wind on Mars, based on joint observations by Tianwen-1 and MAVEN. In our study, MAVEN is positioned near the subsolar magnetopause, while Tianwen-1 is positioned near the high-latitude magnetopause. Both satellites detected three consecutive MHs. Utilizing the crossing signals, we estimated the minimum sizes of these MHs and reconstructed the situation of the satellites passing through the MHs. Due to the initial positions of the satellites and the eccentricity of their trajectories relative to the primary orientation of the MHs, Tianwen-1 experienced delays in detecting the signals from these holes. Additionally, we observed whistler waves in the third MH and identified perpendicular anisotropy as the driver for these waves.

Acknowledgments

We would like to thank the Tianwen-1 and MAVEN teams for providing data access and support. Special thanks to J. E. P. Connerney, D. L. Mitchell, and J. S. Halekas for their contributions in making available data from MAG, SWEA, and SWIA, respectively.

The Tianwen-1/MOMAG data are available at the Lunar and Planetary Data Release System (https://moon.bao.ac.cn/web/enmanager/kxsj?missionName=HX1&zhName=MOMAG&grade=2C). The MOMAG data used in this paper can also be retrieved from the official site of the MOMAG team (http://space.ustc.edu.cn/dreams/tw1_momag/). The MINPA data are available from the Chinese Lunar and Planetary Data Release System (https://moon.bao.ac.cn/web/zhmanager/mars1) upon application. All MAVEN data used in this study are available through the MAVEN Science Data Center (https://lasp.colorado.edu/maven/sdc/public/data/sci/).

This work was supported by NSFC grants 42241113 and 41821003 and "the Fundamental Research Funds for the Central Universities." We express our gratitude to the ISSI-BJ travel grant for team "Understanding Electron-Scale Magnetic Structures in Space Plasmas." The calibration of MOMAG data is supported by NSFC 42130204.

ORCID iDs

H. S. Fu https://orcid.org/0000-0002-4701-7219
Z. Z. Guo https://orcid.org/0000-0002-4479-7045
Y. M. Wang https://orcid.org/0000-0002-8887-3919
Z. Wang https://orcid.org/0000-0002-1720-964X

References

Balikhin, M. A., Sibeck, D. G., Runov, A., & Walker, S. N. 2012, JGRA, 117, A08229
Brain, D. A., Bagenal, F., Acuna, M. H., et al. 2002, JGRA, 107, 1076
Burlaga, L. F., & Lemaire, J. F. 1978, JGR, 83, 5157
Chen, Y., Wu, M., Xiao, S., et al. 2022, FrASS, 9, 858300
Connerney, J. E. P., Espley, J., Lawton, P., et al. 2015, SSRv, 195, 257
Fu, H. S., Cao, J. B., Khotyaintsev, Y. V., et al. 2013a, GeoRL, 40, 6023
Fu, H. S., Cao, J. B., Yang, B., et al. 2011a, JGRA, 116, A10210

Fu, H. S., Chen, F., Chen, Z. Z., et al. 2020a, PhRvL, 124, 095101
Fu, H. S., Grigorenko, E. E., Gabrielse, C., et al. 2020b, ScChD, 63, 235
Fu, H. S., Khotyaintsev, Y. V., André, M., et al. 2011b, GeoRL, 38, L16104
Fu, H. S., Khotyaintsev, Y. V., Vaivads, A., et al. 2012, JGR, 117, A12221
Fu, H. S., Khotyaintsev, Y. V., Vaivads, A., et al. 2013b, NatPh, 9, 426
Fu, H. S., Vaivads, A., Khotyaintsev, Y. V., et al. 2017, GeoRL, 44, 37
Fu, H. S., Xu, Y., Vaivads, A., & Khotyaintsev, Y. V. 2019, APJL, 870, L22
Guo, Z. Z., Fu, H. S., Cao, J. B., et al. 2021, GeoRL, 48, e93826
Guo, Z. Z., Liu, Y. Y., Fu, H. S., et al. 2022, APJ, 933, 128
Halekas, J. S., Taylor, E. R., Dalton, G., et al. 2015, SSRv, 195, 125
Huang, S. Y., Du, J. W., Sahraoui, F., et al. 2017a, JGRA, 122, 8577
Huang, S. Y., Fu, H. S., Yuan, Z. G., et al. 2015, JGRA, 120, 4496
Huang, S. Y., He, L. H., Yuan, Z. G., et al. 2019, ApJ, 875, 113
Huang, S. Y., Lin, R. T., Yuan, Z. G., et al. 2021, ApJ, 922, 107
Huang, S. Y., Sahraoui, F., Yuan, Z. G., et al. 2017b, ApJL, 836, L27
Huang, S. Y., Sahraoui, F., Yuan, Z. G., et al. 2018, ApJ, 861, 29
Huang, S. Y., Wei, Y. Y., Zhao, J. S., et al. 2022, GeoRL, 49, e93813
Huang, S. Y., Zhou, M., Deng, X. H., et al. 2012, AnG, 30, 97
Jakosky, B. M., Lin, R. P., Grebowsky, J. M., et al. 2015, SSRv, 195, 3
Jiang, K., Huang, S. Y., Wei, Y. Y., et al. 2024, GeoRL, 51, e2024GL109685
Jiang, K., Huang, S. Y., Yuan, Z. G., et al. 2020, GeoRL, 47, e88448
Joy, S. P., Kivelson, M. G., Walker, R. J., et al. 2006, JGRA, 111, A12212
Kong, L., Zhang, A., Tian, Z., et al. 2020, E&PP, 4, 333
Liu, K., Hao, X., Li, Y., et al. 2020, E&PP, 4, 384
Liu, Y. Y., Fu, H. S., Liu, C. M., et al. 2019, ApJL, 877, L16
Liu, Y. Y., Fu, H. S., Zong, Q. G., et al. 2020, GeoRL, 47, e88374
Lucek, E. A., Dunlop, M. W., Balogh, A., et al. 1999, GeoRL, 26, 2159
Madanian, H., Halekas, J. S., Mazelle, C. X., et al. 2020, JGRA, 125, e27198
Mitchell, D., Mazelle, C., Sauvaud, J.-A., et al. 2016, SSRv, 200, 495
Nagy, A. F., Winterhalter, D., Sauer, K., et al. 2004, SSRv, 111, 33
Ramstad, R., Brain, D., Dong, Y., et al. 2020, NatAs, 4, 979
Russell, C. T., Riedler, W., Schwingenschuh, K., et al. 1987, GeoRL, 14, 644
Santolík, O., Parrot, M., & Lefeuvre, F. 2003, RaSc, 38, 1010
Soucek, J., Lucek, E., & Dandouras, I. 2008, JGRA, 113, A04203
Tsurutani, B. T., Lakhina, G. S., Verkhoglyadova, O. P., et al. 2011, JGRA, 116, A02103
Tsurutani, B. T., Smith, E. J., Anderson, R. R., et al. 1982, JGR, 87, 6060
Turner, J. M., Burlaga, L. F., Ness, N. F., & Lemaire, J. F. 1977, JGR, 82, 1921
Wan, W. X., Wang, C., Li, C. L., et al. 2020, NatAs, 4, 721
Wang, G. Q., Volwerk, M., Du, A. M., et al. 2021, ApJ, 921, 153
Wang, G. Q., Xiao, S. D., Wu, M. Y., et al. 2024, JGRA, 129, e2023JA031757
Wang, Y., Zhang, T., Wang, G., et al. 2023, E&PP, 7, 1
Wang, Z., Fu, H. S., Liu, C. M., et al. 2019, GeoRL, 46, 1195
Wang, Z., Fu, H. S., Vaivads, A., et al. 2020, ApJL, 899, L34
Wang, Z., Huang, S. Y., Yuan, Z. G., et al. 2023, ApJ, 957, 108
Wang, Z., Liu, X. Y., Fu, H. S., et al. 2024, ApJ, 960, 45
Wu, M., Chen, Y., Du, A., et al. 2021, ApJ, 916, 104
Xiao, T., Shi, Q. Q., Tian, A. M., et al. 2014, SoPh, 289, 3175
Xiao, T., Shi, Q. Q., Zhang, T. L., et al. 2010, AnG, 28, 1695
Xu, Y., Fu, H. S., Norgren, C., Hwang, K.-J., & Liu, C. M. 2018, PhPl, 25, 072123
Yao, S. T., Shi, Q. Q., Yao, Z. H., et al. 2019, GeoRL, 46, 523
Yu, L., Huang, S. Y., Fu, H. S., et al. 2024, ApJ, 963, 64
Yu, L., Huang, S. Y., Yuan, Z. G., et al. 2021, ApJ, 908, 56
Yu, L., Huang, S. Y., Yuan, Z. G., et al. 2022, JGR, 127, e30505
Yu, Y., Fu, H. S., Cao, J. B., Liu, Y. Y., & Wang, Z. 2022a, ApJ, 926, 199
Yu, Y., Wang, Z., Fu, H. S., & Cao, J. B. 2022b, JGRA, 127, e2022JA030805
Zhang, T. L., Russell, C. T., Baumjohann, W., et al. 2008, GeoRL, 35, L10106
Zhang, X., Angelopoulos, V., Artemyev, A. V., & Liu, J. 2019, GeoRL, 46, 11718
Zhima, Z., Cao, J., Fu, H., et al. 2015, JGRA, 120, 2469
Zou, Z., Wang, Y., Zhang, T., et al. 2023, ScChE, 66, 2396